JOURNAL OF THERMOPHYSICS AND HEAT TRANSFER
Vol. 8, No. 2, April–June 1994

Comparisons Between Monte Carlo Methods and Navier-Stokes Equations for Re-Entry Flows

David R. Olynick*
NASA Ames Research Center, Moffet Field, California 94035
and
Jeff C. Taylor† and H. A. Hassan‡
North Carolina State University, Raleigh, North Carolina 27695

A detailed comparison is made between Navier-Stokes and direct stimulation Monte Carlo calculations for flows near the continuum limit to assess the accuracy of the continuum equations in this regime. Meaningful comparisons require the use of similar physical models. This necessitates the inclusion of a separate rotational energy equation and use of slip boundary conditions. Inclusion of slip boundary conditions resulted in improved agreement between surface properties. Moreover, good agreement was obtained for the various temperatures in the nonequilibrium portion of the flowfield that does not contain the shock region. Departures are noted in the shock region and in regions where thermal diffusion effects are important.

Introduction

IN recent years, there has been an interest in solving re-entry problems geared toward aerobraking applications. Aerobraking maneuvers have been proposed for a manned mission to Mars and various orbital transfer vehicles. These vehicles operate in both continuum and noncontinuum regimes. Thus, flow calculations have been performed using both particle and continuum methods.

The direct simulation Monte Carlo method (DSMC) of Bird is one particle method that has been used extensively to solve re-entry flow problems. The method is valid for both noncontinuum and continuum flow conditions. However, because the computational cost of the method increases as density increases, its application is normally limited to flow conditions near the upper limits of what can be considered a continuum. The Navier-Stokes equations have also been employed to solve problems for these conditions. However, as the continuum limit is approached, the accuracy of the Navier-Stokes equations becomes questionable. Thus, the major objective of this work is to determine the limits of validity of the Navier-Stokes equations by comparing their predictions with the DSMC method.

To make direct comparisons between the DSMC method and Navier-Stokes equations, two issues must be addressed. First, continuum equations must be employed that allow for the separate calculation of the translational, rotational, and vibrational energy modes. In past comparisons of continuum and DSMC solutions,[1-3] it was assumed that the translational and rotational temperatures were equal for the continuum calculations. Moreover, the relaxation rates for the internal modes should match those employed in the DSMC method. Second, slip effects must be included in the Navier-Stokes calculations. Including slip effects requires a detailed treatment of the Knudsen layer at the surface of the vehicle. In the following sections, the continuum equation set employed in this study is described, and predictions are compared with the DSMC method. Moreover, the modeling of the Knudsen layer is discussed.

Received June 17, 1993; presented as Paper 93-2810 at the AIAA 28th Thermophysics Conference, Orlando, FL, July 6–9, 1993; revision received Nov. 2, 1993; accepted for publication Nov. 23, 1993.

*Research Engineer, M/S 234-1. Member AIAA.
†Research Assistant, Mechanical and Aerospace Engineering Department. Student Member AIAA.
‡Professor, Mechanical and Aerospace Engineering Department. Associate Fellow AIAA.

Physical Modeling

In this section, a set of continuum equations is described that is appropriate for re-entry flows near the continuum limit. To eliminate uncertainties in comparing flow solutions, an effort is made to match as closely as possible the physics employed in the computational fluid dynamics (CFD) and DSMC methods. The model equations for aerobraking flowfields have been presented in a number of sources.[3-5] For this study, the following equations will be solved: global mass, momentum and energy, species, rotational and vibrational energy. In axisymmetric coordinates, the above set of equations can be written as follows:

$$\frac{\partial \boldsymbol{U}}{\partial t} + \frac{\partial \boldsymbol{F}}{\partial x} + \frac{1}{y}\frac{\partial (y\boldsymbol{G})}{\partial y} = \boldsymbol{W} \tag{1}$$

where

$$\boldsymbol{U} = \begin{bmatrix} \rho \\ \rho_2 \\ \vdots \\ \rho_n \\ \rho u \\ \rho v \\ \rho E_r \\ \rho E_v \\ \rho E \end{bmatrix}$$

$$\boldsymbol{F} = \begin{bmatrix} \rho u \\ \rho_2(u + V_{x2}) \\ \vdots \\ \rho_n(u + V_{xn}) \\ \rho u^2 + p + \tau_{xx} \\ \rho uv + \tau_{xy} \\ E_r u + q_{rx} + \Sigma_{s=\text{mol}}\, \rho_s e_{rs} V_{xs} \\ E_v u + q_{vx} + \Sigma_{s\text{-mol}}\, \rho_s e_{vs} V_{xs} \\ (E + p + \tau_{xx})u + \tau_{xy} v + q_x + q_{rx} + q_{vx} + \Sigma_s^n\, \rho_s h_s V_{xs} \end{bmatrix}$$

$$G = \begin{bmatrix} \rho v \\ \rho_2(v + V_{y2}) \\ \vdots \\ \rho_n(v + V_{yn}) \\ \rho uv + \tau_{xy} \\ \rho v^2 + p + \tau_{yy} \\ E_r v + q_{ry} + \Sigma_{s=\text{mol}} \rho_s e_{rs} V_{ys} \\ E_v v + q_{vy} + \Sigma_{s=\text{mol}} \rho_s e_{vs} V_{ys} \\ (E + p + \tau_{yy})v + \tau_{xy} u + q_y + q_{ry} + q_{vy} \\ + \Sigma_s^n \rho_s h_s V_{ys} \end{bmatrix}$$

$$W = \begin{bmatrix} 0 \\ w_2 \\ \vdots \\ w_n \\ 0 \\ (p - \tau_{\theta\theta})/y \\ Q_{T-r} + \Sigma_{s=\text{mol}} w_s e_r s \\ Q_{T-v} + \Sigma_{s=\text{mol}} w_s e_v s \\ 0 \end{bmatrix}$$

In the above equations, $V_{(s,v)s}$ is the diffusion velocity of species s in the x or y direction. $E_{(r,v)}$ is the total rotational or vibrational energy per unit volume. $e_{(r,v)s}$ is the rotational or vibrational energy per unit mass of species s. w_s is the production rate of species s. The various Q terms are the result of coupling between the various energy modes and the chemistry. The modeling of the source terms in the above equations will be discussed in the following paragraphs.

The rotational modes are assumed to be fully excited. Therefore, the rotational energy is given by

$$E_r = \sum_{s=\text{mol}} \rho_s e_{rs}, \qquad e_{rs} = \frac{R_{\text{univ}}}{M_s} T_r = R_s T_r$$

where R_{univ} is the universal gas constant, and M_s is the molecular weight of species s. For this study, only translational-rotational coupling, Q_{T-r}, was considered. Q_{T-r} is modeled by a Landau-Teller type expression as follows:

$$Q_{T-r} = \sum_{s=\text{mol}} \rho_s R_s \frac{(T - T_r)}{\tau_r} \tag{2}$$

where

$$\tau_r = Z_r \tau_c, \qquad \tau_c = \frac{\pi}{4} \frac{\mu}{p}, \qquad Z_r = 5 \tag{3}$$

In the above equation, τ_c is the mean collision time, μ is the mixture viscosity, and Z_r is the ratio (τ_r/τ_c). Z_r represents the number of collisions it takes a molecule to reach rotational equilibrium. The value of Z_r was set equal to five to agree with the DSMC calculation.

The vibrational energy for each species is obtained using a harmonic oscillator model. Thus, the total vibrational energy is given by

$$E_v = \sum_{s=\text{mol}} \rho_s e_{vs}, \qquad e_{vs} = \frac{R_s \theta_{vs}}{\exp(\theta_{vs}/T_{vs}) - 1} \tag{4}$$

where θ_{vs} is the characteristic vibrational temperature of each species. The translational-vibrational coupling, Q_{T-v} is modeled using a Landau-Teller expression as

$$Q_{T-v} = \sum_{s=\text{mol}} \rho_s \frac{e_{vs}(T) - \mathrm{e}_{vs}(T_v)}{\tau_{vs}} \tag{5}$$

$$\tau_{vs} = \tau_{s_{L-T}} + \tau_{cs} \tag{6}$$

In the above equation, $\tau_{s_{L-T}}$ is a molar-averaged relaxation time for each species based on the Millikan-White formula,[6] and τ_{cs} is the high temperature correction to the Millikan-White formula suggested by Park.[5]

In the DSMC method, energy exchange during an inelastic collision is treated using the Larsen-Borgnakke phenomenological model.[7] The relaxation rate for the translational-rotational coupling is proportional to the rotational collision number and the average collision frequency in the cell. A similar procedure is used to calculate the translational-vibrational coupling. The vibrational collision numbers are calculated to produce a relaxation rate[8] that agrees with the Millikan and White formulation described in the previous paragraph. Therefore, using the above formulations, the rotational and vibrational relaxation rates are similar for both methods.

The shear stresses, heat conduction, and diffusion terms are modeled using formulations standard to the Navier-Stokes equations. The shear stresses are assumed to be proportional to the first derivatives of the velocities. Therefore, using the Stokes assumption, the shear stresses are given by

$$\tau_{ij} = -\mu \left(\frac{\partial u_i}{\partial x_j} + \frac{\partial u_j}{\partial x_i} \right) - \lambda \frac{\partial u_k}{\partial x_k} \delta_{ij}, \qquad \lambda = -\frac{2}{3} \mu \tag{7}$$

The heat conduction vectors are assumed to be given by the Fourier heat law

$$q_j = -k_t \frac{\partial T}{\partial x_j}, \qquad q_{rj} = -k_r \frac{\partial T_r}{\partial x_j}, \qquad q_{vj} = -k_v \frac{\partial T_v}{\partial x_j} \tag{8}$$

The diffusion velocity of species s is assumed to be governed by Fick's law

$$\rho_s V_{sj} = -\rho D_s \frac{\partial c_s}{\partial x_j} \tag{9}$$

where D_s and c_s are the diffusion coefficient and mass fraction of species s. The transport coefficients for the above equations, μ, $k_{t,r,v}$, and D_s, are obtained from the cross section data of Yos as defined in Ref. 9. In the DSMC method, a variable hard sphere (VHS) collision model[10] is employed. At the high temperatures of interest here, viscosity coefficients calculated from the VHS model approximate closely those employed in the continuum equations. The DSMC calculations do assume that all collisions are governed by the same interaction law.

For this study, the first 19 reactions from the chemistry model given by Bird[11] are employed in both the CFD and DSMC calculations. The model is valid for a five-species air model consisting of N_2, O_2, NO, N, and O. The reactions considered are as follows:

(1) $N_2 + M \Leftrightarrow N + N + M$
(2) $O_2 + M \Leftrightarrow O + O + M$
(3) $NO + M \Leftrightarrow N + O + M$
(4) $N_2 + O \Leftrightarrow NO + N$
(5) $NO + O \Leftrightarrow O_2 + N$

For reactions 1–3, the recombination reaction is not considered for both methods. For the continuum method, the reaction rates are assumed to be only a function of the translational temperature.

The probabilities or cross sections needed in DSMC to determine whether or not a certain collision will result in a chemical reaction are energy dependent. The relation between the cross section or probability and the rate can be written as[10]

$$k_f(T_a) = \overline{\sigma_T c_r} \int_{(E_a/kT_a)}^{\infty} Pr(E, E_a) f\left(\frac{E}{kT_a}\right) \mathrm{d}\left(\frac{E}{kT_a}\right)$$

In the above equation k_f is the forward rate, σ_T is the total cross section, c_r is the relative velocity, Pr is the cross section or probability, and f is the distribution function. T_a is some temperature which can be the translational temperature or some other combination of temperatures. The cross sections used in the DSMC method are such that when f is Maxwellian at some T_a, then the measured rate is recovered. The choice of T_a is model-dependent. Thus, in the Park model, T_a is written as $\sqrt{TT_v}$. As a result, comparisons that are reasonable for one choice of T_a may not be acceptable if another choice of T_a is employed. Moreover, if one choice gives a good agreement with DSMC in a given problem, results should not be interpreted as an endorsement of the model. This is because the distribution function for flows in thermal and chemical nonequilibrium may not be Maxwellian.

Boundary Conditions

In this section, the no-slip and slip boundary conditions used in the continuum calculations are described and compared with the DSMC boundary conditions. The no-slip conditions typically employed in Navier-Stokes calculations are as follows. The average velocity at the surface boundary is assumed to be zero and the wall temperature is assumed to be constant. Thus

$$U_s = U_w = 0 \qquad T_s = T_w \tag{10}$$

where the subscripts s and w denote properties at the surface boundary and wall.

The wall is assumed to have a finite catalytic coefficient. Therefore, the species mass flux at the wall is related to the rate of diffusion towards the surface as follows[5]:

$$\left(\rho D \frac{\partial c_i}{\partial \eta}\right)_w = (\rho_i K_i)_w \tag{11}$$

where η denotes the direction normal to the surface. The reaction rate at the wall is given by

$$K_{wi} = \gamma_i \sqrt{(kT_w/2\pi m_i)} \tag{12}$$

where γ_i is the fraction of species i consumed at the surface, k is the Boltzmann constant, and m_i is the mass of species i. A more accurate representation of the surface conditions for flows near the continuum limit requires a detailed treatment of the Knudsen layer. The representation of the Knudsen layer is described in the following paragraphs.

The Knudsen layer is defined as the region of the flow within one mean free path of the surface. Within the layer, the flow is no longer a continuum and the Navier-Stokes equations are invalid. However, it is possible to relate the conditions at the surface boundary to properties at the edge of the Knudsen layer. The edge properties provide the boundary conditions for the Navier-Stokes equations. The relationships between the edge and wall properties are known as slip boundary conditions. The slip boundary conditions used in this study are derived from Ref. 12. The equations were obtained by neglecting higher-order terms and employing a "thin-layer" assumption.

The tangential velocity at the edge of the Knudsen layer is given as

$$U_s = \frac{\sqrt{\frac{\pi}{2}}\left(\frac{\mu}{\rho}\frac{\partial U}{\partial \eta} - \kappa U\right)_s}{\sum_i [c_i^s \sqrt{kT_s/m_i})]} \tag{13}$$

where κ is the surface curvature and s denotes properties at the edge of the Knudsen layer. The temperature at the edge of the Knudsen layer is given as

$$\frac{T_s}{T_w} = \frac{-\frac{\sqrt{\pi}}{\bar{n}_s}\sum_i \left(\frac{m_{iy}}{m_i}\right) + \sum_i \left(\sqrt{\frac{2kT_s}{m_i}}\frac{\bar{m}_s}{m_i} c_i^s\right)}{-\frac{\sqrt{\pi}}{2}\left(\frac{k_t}{p}\frac{\partial T}{\partial \eta}\right)_s - \frac{5}{4}\sum_i \left(\frac{M_{iy}}{\bar{n}m_i}\right)_s + \sum_i \left(\sqrt{\frac{2kT_s}{m_i}}\frac{\bar{m}_s}{m_i} c_i^s\right)} \tag{14}$$

where k_t is the translational conductivity and $\bar{n}$ is the total number density. The quantities M_{iy} and $\bar{m}$ are defined as follows:

$$\begin{aligned} \mathrm{M}_{Ay} &= -\rho_A^w K_{wA} \qquad A = \mathrm{O}, \mathrm{N} \\ \mathrm{M}_{\mathrm{N}_2 y} &= -\mathrm{M}_{\mathrm{N}y} \qquad \mathrm{M}_{\mathrm{O}_2 y} = -\mathrm{M}_{\mathrm{O}y} \end{aligned} \tag{15}$$

$$\bar{m} = \left(\sum_i \frac{c_i}{m_i}\right)^{-1} \tag{16}$$

Finally, the species mass fractions at the edge of the Knudsen layer are given as

$$\left(\rho D \frac{\partial c_i}{\partial \eta}\right)_s = (\rho_i \phi_i)_s \tag{17}$$

where

$$\begin{aligned} \phi_i &= \frac{\gamma_i}{2 - \gamma_i}\sqrt{\frac{2kT_s}{\pi m_i}} \qquad i = \mathrm{N}, \mathrm{O} \\ \phi_i &= 0 \qquad i = \mathrm{NO} \\ \phi_{\mathrm{N}_2} &= -\phi_{\mathrm{N}} \qquad \phi_{\mathrm{O}_2} = -\phi_{\mathrm{O}} \end{aligned} \tag{18}$$

The above formulation was derived to be compatible with Fick's diffusion law.

In the DSMC method, it assumed that the surface is diffuse, fully accommodating, and at a fixed temperature. When a particle strikes a diffuse surface, the reflected velocity of the particle is independent of its incident velocity. Because the surface is fully accommodating, the reflected velocities are distributed according to a half-range equilibrium Maxwellian velocity distribution at the wall temperature.[13] Also, the internal modes of the particle take on an energy characteristic of the wall temperature. The wall temperature used in the DSMC method corresponds to the wall temperature utilized in Eq. (10). Wall catalytic condition is implemented by allowing a certain percentage of the atoms that hit the surface to recombine. This percentage corresponds to the γ parameter defined in Eqs. (12) and (18).

Results

The major objective of this study is to determine the range of validity of the Navier-Stokes equations near the continuum limit. To meet this objective, the 1631- and 1634-s flight conditions from the Project Fire II experiment[14,15] are calculated. Data for these conditions are given in Table 1. The velocity, wall temperature, and altitude were obtained from the experimental data. Data for the density and mole fractions were obtained from the 1962 standard atmosphere. The values of γ were chosen to be consistent with the materials used in the Project Fire II experiment.[16]

The criterion for determining whether or not the Navier-Stokes equations should be used to describe the above flow is determined from consideration of the local Knudsen number. The Knudsen number Kn is defined as

$$Kn = \lambda/L \tag{19}$$

Table 1 Fire II flow conditions

Time	1631 s	1634 s
Altitude	84.6 km	76.42 km
V_∞	11.37 km/s	11.36 km/s
ρ_∞	8.569×10^{-6} kg/m^3	3.50836×10^{-5} kg/m^3
T_∞	180.65 K	194.602 K
n_∞	1.782×10^{20} part/m^3	7.29422×10^{20} part/m^3
$Y_{O_2\infty}$	0.2372	0.2372
$Y_{N_2\infty}$	0.7682	0.7628
T_{wall}	460 K	615 K
Kn_∞	0.01	0.0025
γN_2	0.02	0.02
γO_2	0.02	0.02
γNO	0	0

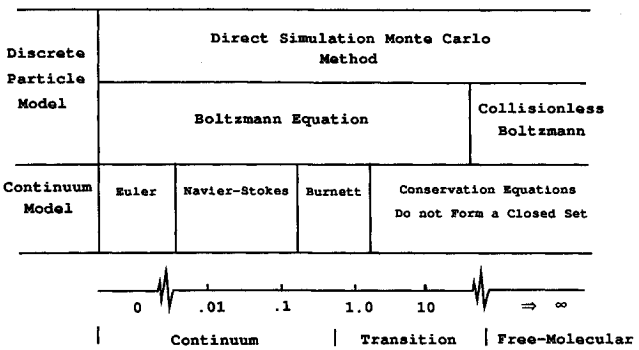

Fig. 1 Range of validity for the particle and continuum methods vs local Knudsen number.

where λ is the mean free path and L is a characteristic length in the flow. In this study, a local L is defined from the local density gradient as

$$L^{-1} = \frac{1}{\rho}\frac{\partial \rho}{\partial x} \tag{20}$$

Figure 1 shows the range of validity for the continuum and discrete particle models, and the various flow regimes as a function of the local Knudsen number. It can be seen in the figure that a continuum approximation is valid for local Knudsen numbers of about 0.1 and below.[17]

For the 1634 and 1631 cases, the freestream Knudsen numbers based on the nose radius of the vehicle [$Kn_\infty = (\lambda_\infty/R_n)$] are equal to 0.0025 and 0.01, respectively. The magnitudes of Kn_∞ are much less than 0.1. Thus, it might be assumed for these cases that the Navier-Stokes equations are an accurate description of the flow. However, examination of the local Knudsen numbers along the stagnation streamline shows that, in the shock region and near the surface, they are one to two orders of magnitude higher than in the freestream. Thus, it is expected that the accuracy of the Navier-Stokes will suffer in these regions of the flow.

The use of the continuity equation in place of one of the species equations, conserves mass. However, when species conservation equations are employed, there is no assurance that elements will be conserved. This is especially true if species-dependent diffusion coefficients are used for which the requirement $\Sigma\, \rho_s V_s = 0$ is not met. To insure that elements are conserved, one of the species conservation equations was replaced by an element conservation equation. Moreover, the above requirement on diffusion velocities was met.[18] Therefore, in the present calculations, conservation of both mass and element are met.

Table 2 gives a summary of grids employed. In the first set of calculations a baseline is established for comparing the DSMC and Navier-Stokes calculations. Thus, the typical boundary conditions employed in most Navier-Stokes calculations, i.e., no slip conditions, are utilized. These results are compared with calculations employing slip boundary conditions to determine the effect of the Knudsen layer on the flow properties.

Table 2 Computational mesh sizes

Time	Tangential × normal
DSMC	
1631 s	16 × 231
1634 s	31 × 601
CFD	
1631 s	33 × 126
1634 s	
Unadapted	33 × 99
Adapted	33 × 99
Doubled	33 × 197

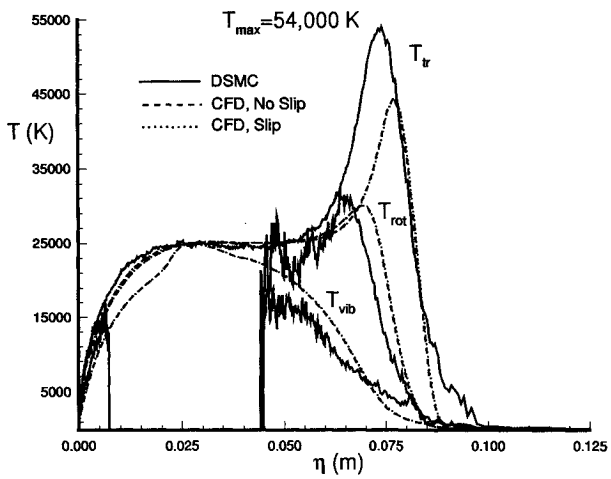

Fig. 2 Comparison of temperatures along the stagnation line for Fire II-1634.

Figure 2 is a comparison of the translational, rotational, and vibrational temperatures along the stagnation line for the 76-km case. The grid used in the CFD calculation is denoted as "unadapted" in Table 2. Overall, qualitative agreement is good. However, DSMC indicates a higher translational temperature and a thicker shock region. Although not shown, slip effects were only discernible next to the surface. The figure illustrates one of the difficulties involved in comparing DSMC and Navier-Stokes calculations. As is seen from the figure, T_r and T_v results from DSMC calculations are not shown in certain regions of the flow. In other regions, they are characterized by large fluctuations or noise. This is caused by the almost complete dissociation behind the shock. The rotational and vibrational temperatures in the DSMC calculation are generated by sampling the internal energies of the simulated molecules. Since dissociation was nearly complete for this case, the sample size of the molecular species was very small and the predicted temperatures were widely scattered. The widely scattered data points were filtered from the DSMC solution.

Discrepancies in the prediction of the shock structure originate from a number of sources. One source of error for the continuum calculation is that the linear relations used to model the shear stresses and heat conduction are inaccurate in the shock region. Another possible source of error in the CFD calculation could result from grid resolution effects. The DSMC method employs a much finer grid. Thus, the strong gradients within the shock are more resolved in the DSMC calculation. To determine grid resolution effects, CFD solutions were calculated on two additional grids at the 76-km conditions. First, an adapted grid was generated from the previous continuum

solution. The number of grid points normal to the body was kept fixed, but points were clustered in the shock and near the body. Second, the number of normal grid points on the first grid were doubled by interpolating between points. The new grids are denoted as adapted and doubled in Table 2.

The CFD slip and no-slip calculations were repeated on each of the new grids and compared with the CFD results on the unadapted grid. The calculations on all of the grids yielded nearly identical results. Figure 3 shows a comparison of the CFD no-slip solutions on the various grids with the DSMC results in the shock region. The adapted and doubled calculations show a slightly higher peak translational temperature and lower rotational temperature in the shock relative to the unadapted results. The slightly changed temperatures in the shock were the only differences obtained on the adapted and doubled grids using both slip and no-slip conditions. Therefore, in the following comparisons for the 76-km case, only the CFD results employing the unadapted grid are presented. Next, the effects of slip modeling are examined.

Figures 4–6 are plots of the various temperatures near the surface along the stagnation line. It can be seen in the figures that the inclusion of slip boundary conditions produces results that agree better with the DSMC calculation. The best improvement is obtained for the translational and rotational temperatures. Agreement between the vibrational temperatures is poor. The poor agreement between the vibrational temperatures may be the result of the high degree of dissociation behind the shock. The comparison for the 84-km results in which the dissociation level is lower is improved. These results are described later in this section.

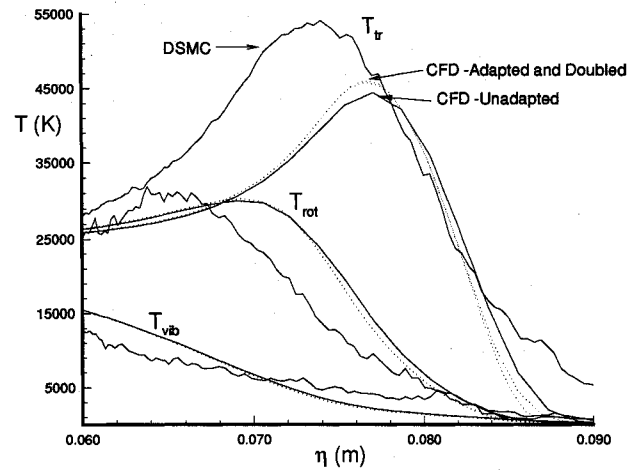

Fig. 3 Grid resolution effects on the stagnation line temperatures for Fire II-1634.

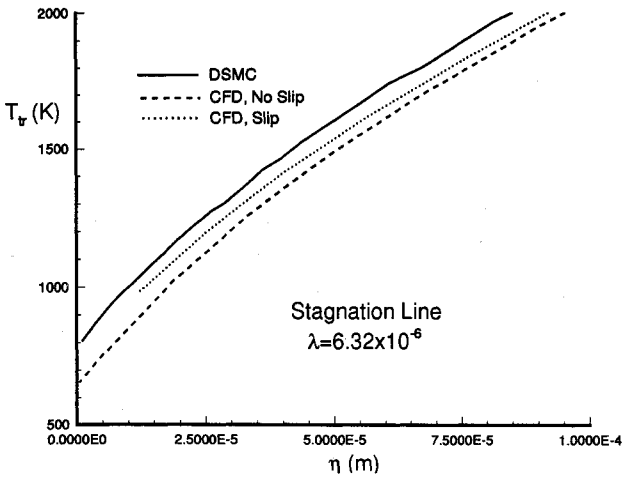

Fig. 4 Translational temperatures along the stagnation line near the surface for Fire II-1634.

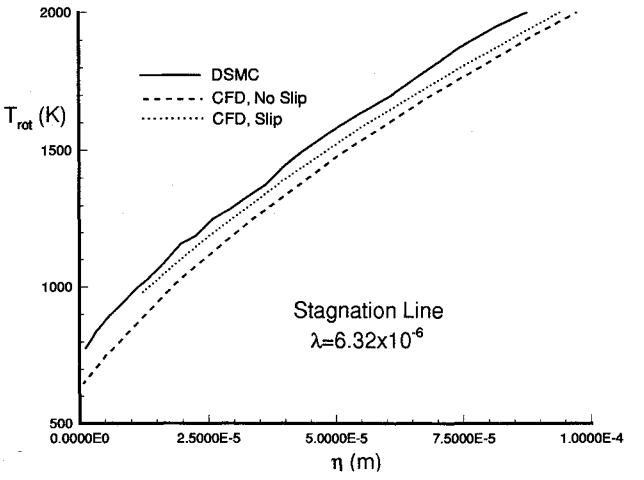

Fig. 5 Rotational temperatures along the stagnation line near the surface for Fire II-1634.

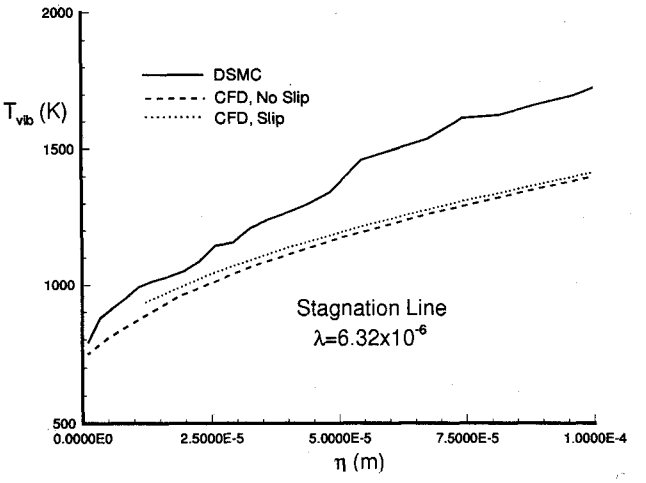

Fig. 6 Vibrational temperatures along the stagnation line near the surface for Fire II-1634.

It should be noted in Figs. 4–6 that the CFD slip results are shifted relative to the surface. The slip boundary equations give properties at the edge of the Knudsen layer, whereas the no-slip equations give results at the surface of the vehicle. Since both the no-slip and slip calculations were performed on the same grid, the slip results were shifted by one mean free path. A mean free path is the assumed width of the Knudsen layer, and its magnitude is given in the figure. Next, the mole fractions along the stagnation stream line are examined.

Figure 7 is a plot of the various mole fractions along the stagnation streamline. It can be seen that the methods are in good agreement except in the nonequilibrium portion of the shock. Figure 8 indicates the manner in which the density increases through the shock region. Since the dissociation rate increases with density and temperature, and since the temperature shock precedes the density shock, DSMC predicts a higher dissociation rate initially. Later, the faster rise of density predicted by the continuum solution results in increased dissociation. The resulting slower dissociation rate indicated for the DSMC results is responsible for the peak translational temperature indicated in Fig. 2. Since the reaction rates for the continuum calculations were based on the translational temperature, one can mimic delayed dissociation effects by employing a two-temperature dissociation model such as those developed by Park[19] or Olynick and Hassan.[18] Thus, employing one of these models would improve the agreement between the methods.

Figure 9 is a comparison of the NO mole fraction along the stagnation line, which is of interest for radiation signature

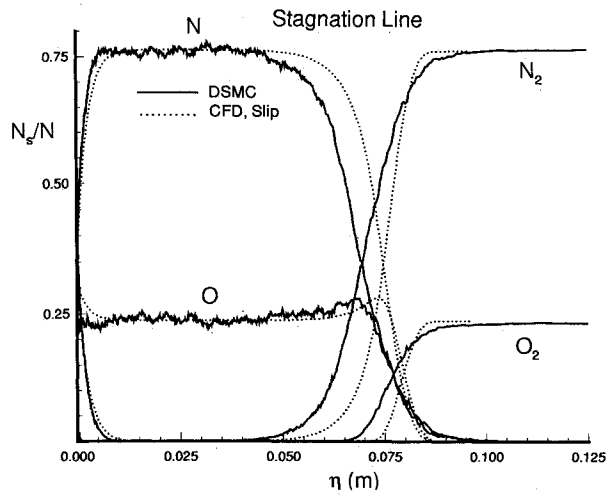

Fig. 7 Various mole fractions along the stagnation line for Fire II-1634.

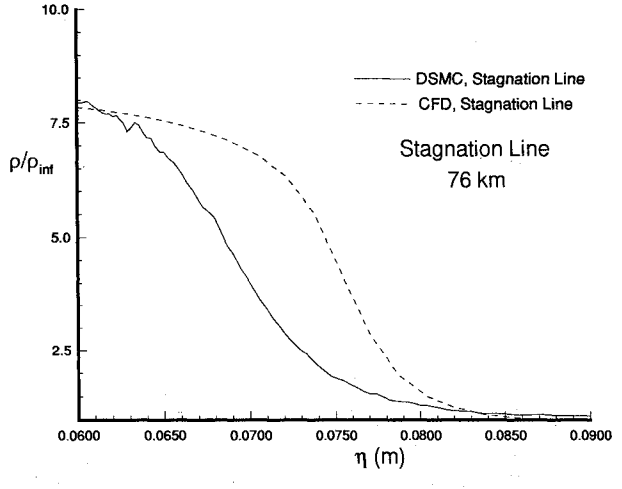

Fig. 8 Density along the stagnation line for Fire II-1634.

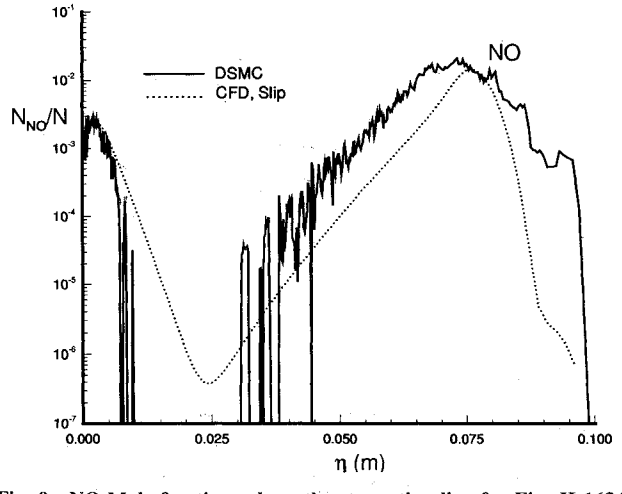

Fig. 9 NO Mole fractions along the stagnation line for Fire II-1634.

calculations.[20] The DSMC calculation produced more NO in the shock region, which is consistent with its higher translational temperature. Figure 10 is a plot of the mole fractions near the surface along the stagnation line. The effects of concentration slip are minimal. However, the calculated values of the O and N_2 mole fractions for the methods differ significantly in this region. This result can be explained by examining the elemental mass fractions of N and O along the stagnation line for the DSMC solution. These plots are shown in Fig. 11. It can be seen in the figure that the elemental mass

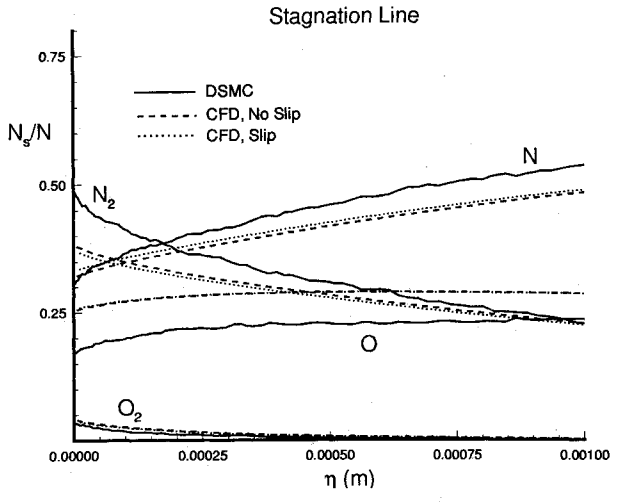

Fig. 10 Various mole fractions along the stagnation line near the surface for Fire II-1634.

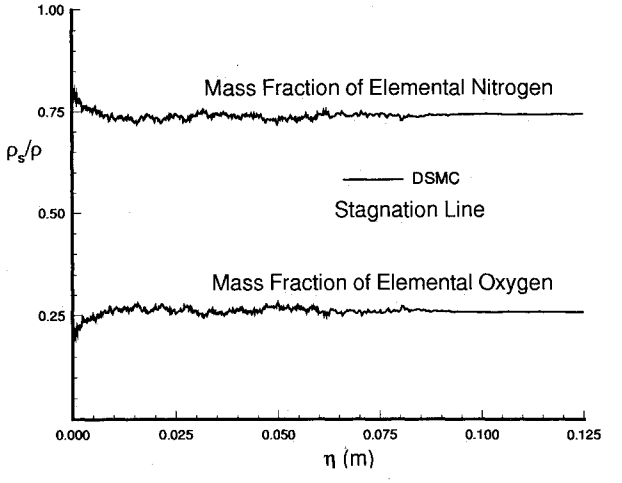

Fig. 11 DSMC elemental mass fractions along the stagnation line for Fire II-1634.

fraction of N increases as the body is approached. This phenomena is a result of thermal diffusion. Thermal diffusion causes the heavier particles to be concentrated in the cooler regions of the flow.[21] Since the wall is cold, more N_2 remains close to the body, which increases the elemental mass fraction of N. For the CFD solutions, the elemental mass fractions are constant because thermal diffusion effects were neglected. Thus, for the CFD calculation, the mole fractions of N_2 are lower, and O are higher near the surface. Differences in the mole fractions were observed along the entire surface of the vehicle.

In Fig. 12, the convective heating is compared along the surface of the vehicle. The incorporation of the slip boundary conditions improves the agreement between the DSMC and CFD methods. However, the predicted heating for DSMC calculation is lower than the CFD result. The maximum difference in the heating along the body between the CFD-slip and DSMC cases is less than 10%. The lower heating for the DSMC case could result from thermal diffusion. Since the mass fraction of O is lower near the surface for the DSMC as a result of thermal diffusion, less O is available to recombine at the surface. Thus, the lower recombination rate reduces the heating for the DSMC case. Next, a few comparisons of the 84-km results are discussed.

Figure 13 shows a comparison of the various temperatures along the stagnation line for the 84-km conditions. Although DSMC predicts a thicker shock region, the various temperatures are in somewhat better agreement than that for the 76-km case. Figure 14 compares the various mole fractions in

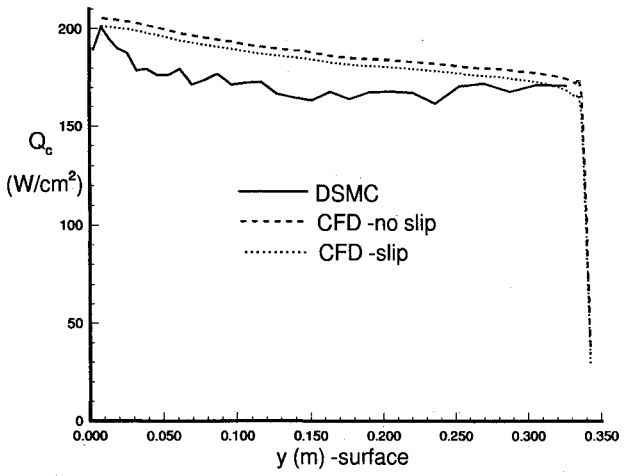

Fig. 12 Convective heating rates along the surface for Fire II-1634.

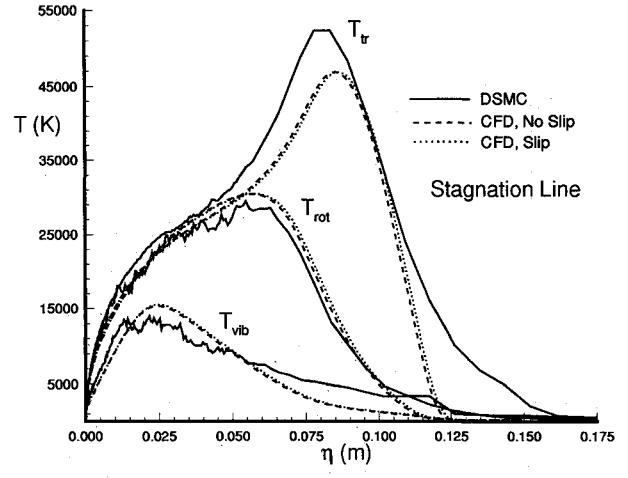

Fig. 13 Comparison of temperatures along the stagnation line for Fire II-1631.

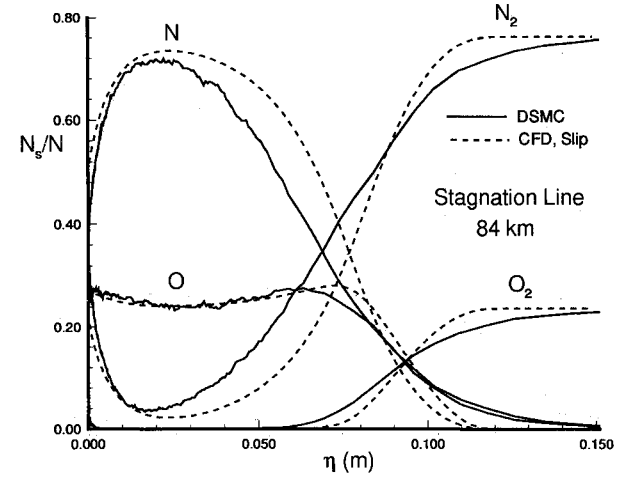

Fig. 14 Number density along the stagnation line for Fire II-1631.

the shock region. The thicker temperature shock predicted by the DSMC results in increased dissociation initially as a result of the increased temperature. This has the tendency to reduce the peak temperature. Later, the higher density predicted by the continuum calculations results in increased dissociation. Because the overall density is reduced when compared to the 76-km case, dissociation is reduced. As a result, we now have a meaningful sample of molecules which makes it possible to calculate smooth vibrational and rotational temperatures.

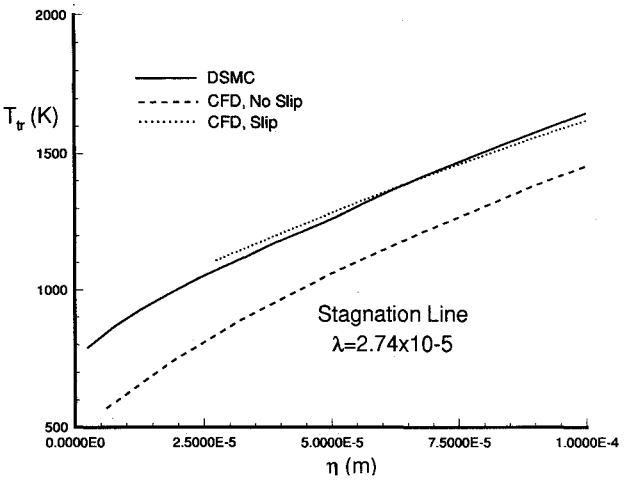

Fig. 15 Translational temperatures along the stagnation line near the surface for Fire II-1631.

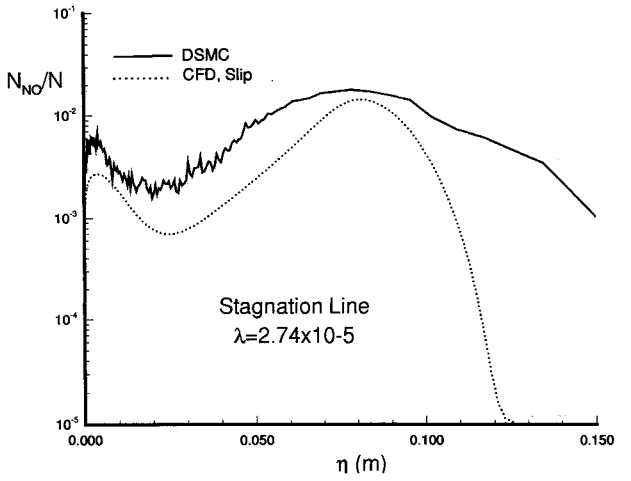

Fig. 16 Comparison of NO mole fractions along the stagnation line for Fire II-1631.

Figure 15 is a comparison of the translational temperatures near the stagnation point. The agreement between the CFD-slip results and the DSMC are excellent in this region. Similar results were obtained for both the rotational and vibrational temperatures. Figure 16 is a comparison of the NO mass fractions along the stagnation line. Because of the reduced dissociation, a more meaningful comparison is possible. Finally, comparisons of the other flow variables are somewhat similar to comparisons for the 76-km case.

Concluding Remarks

We have made a conscious effort in this investigation to employ, to the extent possible, similar physical models in both the Navier-Stokes and DSMC calculations. Inclusion of slip boundary conditions improved the agreement between the two methods. Moreover, good agreement was noted in the regions where the local Knudsen number is less than 0.1 in the presence of chemical and thermal nonequilibrium.

Problems may arise in the presence of both chemical and thermal nonequilibrium if minor species are present. DSMC may require an unacceptable number of simulated molecules and samples in order to calculate meaningful averages. Thus, meaningful comparisons of flow properties of these minor species may not be possible. This issue becomes critical when nonequilibrium radiation is considered.

Thermal diffusion effects are important for highly cooled surfaces. As a result, future Navier-Stokes codes need to incorporate this important physical phenomena.

Acknowledgments

This work is supported in part by NASA's Cooperative Agreement NCCI-112 and the Mars Mission Research Center funded by NASA Grant NAGW-1331. Part of the computer time was provided by the North Carolina Supercomputer Center. One of the authors, David Olynick, would also like to acknowledge some helpful discussions with Forrest Lumpkin and Brian Haas.

References

[1]Gupta, R. N., and Simmonds, A. L., "Hypersonic Low-Density Solutions of the Navier-Stokes Equations with Chemical Nonequilibrium and Multicomponent Surface Slip," AIAA Paper 86-1349, June 1986.

[2]Gnoffo, P. A., "A Code Calibration Program in Support of the Aeroassist Flight Experiment," AIAA Paper 89-1673, June 1989.

[3]Gnoffo, P. A., Gupta, R. N., and Shinn, J. L., "Conservation Equations and Physical Models for Hypersonic Air Flows in Thermal and Chemical Nonequilibrium," NASA TP-2867, Feb. 1989.

[4]Candler, G. V., "The Computation of Weakly Ionized Hypersonic Flows in Thermo-Chemical Nonequilibrium," Ph.D. Dissertation, Stanford Univ., Stanford, CA, 1988, pp. 9–32.

[5]Park, C., *Nonequilibrium Hypersonic Aerothermodynamics*, Wiley, New York, 1990, pp. 119–143.

[6]Millikan, R. C., and White, D. R., "Systematics of Vibrational Relaxation," *Journal of Chemical Physics*, Vol. 39, No. 12, 1963, pp. 3209–3213.

[7]Borgnakke, C., and Larsen, P. S., "Statistical Collision Model for Monte Carlo Simulation of Gas Mixtures," *Journal of Computational Physics*, Vol. 18, No. 3, 1975, pp. 405–420.

[8]Olynick, D. P., Moss, J. N., and Hassan, H. A., "Monte Carlo Simulation of Re-Entry Flows Using a Bimodal Vibration Model," *Journal of Thermophysics and Heat Transfer*, Vol. 4, No. 3, 1990, pp. 273–277.

[9]Gupta, R. N., Yos, J. M., Thompson, R. A., and Lee, K.-P., "A Review of Reaction Rates and Thermodynamic and Transport Properties for an 11-Species Air Model for Chemical and Thermal Nonequilibrium Calculations to 30000 K," NASA Reference Publication 1232, Aug. 1990.

[10]Bird, G. A., "Monte Carlo Simulation in an Engineering Context," *Rarefied Gas Dynamics*, Vol. 74, Pt. I, edited by S. S. Fisher, Progress in Astronautics and Aeronautics, AIAA, New York, 1981, pp. 239–255.

[11]Bird, G. A., "Nonequilibrium Radiation During Reentry at 10 km/s," AIAA Paper 87-1543, June 1987.

[12]Gupta, R. N., Scott, C. D., and Moss, J. N., "Slip-Boundary Equations for Multicomponent Nonequilibrium Airflow," NASA TP-2452, Nov. 1985.

[13]Bird, G. A., *Molecular Gas Dynamics*, Oxford Univ. Press, London, 1976.

[14]Cauchon, D. L., "Radiative Heating Results from the Fire II Flight Experiment at Reentry Velocity of 11.4 km/s," NASA TM X-1402, July 1967.

[15]Cornette, E. S., "Forebody Temperatures and Calorimeter Heating Rates Measured During Project Fire II Reentry at 11.35 km/s," NASA TM X-1305, Nov. 1966.

[16]Taylor, J. C., Carlson, A. B., and Hassan, H. A., "Monte Carlo Simulation of Reentry Flows with Ionization," AIAA Paper 92-0493, Jan. 1992.

[17]Bird, G. A., "Low-Density Aerothermodynamics," AIAA Paper 85-0994, June 1985.

[18]Olynick, D., and Hassan, H., "A New Two-Temperature Dissociation Model for Reacting Flows," AIAA Paper 92-2943, July 1992.

[19]Park, C., "Assessment of a Two-Temperature Kinetic Model for Dissociating and Weekly Ionizing Nitrogen," *Journal of Thermophysics and Heat Transfer*, Vol. 2, No. 1, 1988, pp. 8–16.

[20]Candler, G., Boyd, I., Levin, D., Moreau, S., and Erdman, P., "Continuum and DSMC Analysis of Bow Shock Flight Experiments," AIAA Paper 93-0275, Jan. 1993.

[21]Bird, G. A., "Thermal and Pressure Diffusion Effects in High Altitude Flows," AIAA Paper 88-2732, June 1988.